Experimental studies of atomic structure, electronic structure, and the electronic transport mechanism in amorphous Al-Cu-Y and Mg-Cu-Y ternary alloys

T. Fukunaga, H. Sugiura, N. Takeichi, and U. Mizutani
Department of Crystalline Materials Science, Nagoya University, Furo-cho, Chikusa-ku, Nagoya 464-01, Japan
(Received 1 April 1996)

The local atomic structure in the amorphous $Al_x(Cu_{0.4}Y_{0.6})_{100-x}$ and $Mg_x(Cu_{0.4}Y_{0.6})_{100-x}$ ($0 \leqslant x \leqslant 85$) alloys was determined by neutron-diffraction experiments. The electronic structure near the Fermi level was determined using the same samples by means of x-ray photoemission spectroscopy and soft x-ray spectroscopy. Both sets of data are combined to determine self-consistently and uniquely the local atomic structure in both Al- and Mg-based amorphous alloys. The bonding nature and resulting atomic environment are found to depend significantly on whether the third element is Al or Mg. Based on the atomic and electronic structures thus derived, we could interpret the Al or Mg concentration dependence of the crystallization temperature, electronic specific-heat coefficient, and also that of the resistivity value of 300 K. The origin of the appearance of a positive Hall coefficient observed in the Al-based amorphous alloys but not in the Mg-based amorphous alloys is also briefly discussed. [S0163-1829(96)05729-3]

I. INTRODUCTION

The electron-transport properties of nonmagnetic amorphous alloys reflect well the band structure at the Fermi level E_F, particularly when the resistivity is high enough to reduce a mean free path of electrons at E_F to an average atomic distance.[1] Under such circumstances, the d-electron conduction becomes essential in amorphous alloys consisting of the late transition metal (LT) and early transition metal (ET), in which the density of states at E_F is dominated by the ET d states. An introduction of divalent Mg and trivalent Al into the LT-ET amorphous alloy allows us to change the d-electron-like density of states to the sp-electron-like ones and, hence, offers unique opportunities for studying the scattering mechanism in a disordered system throughout the d- to sp-conduction regimes.

The atomic structure,[2] electronic structure,[3–6] and electron-transport properties[3–7] have been studied in a large number of amorphous Al-LT-ET and Mg-LT-ET (LT=Ni and Cu, ET=Ti, Y, Zr, La) alloys. An addition of Al into the amorphous Ni-Zr alloy, for example, results in an increase in resistivity, a sharp decrease in the electronic specific-heat coefficient and a reversal in a sign of the Hall coefficient from a negative to a positive value.[3,4] On the other hand, the resistivity decreases and the Hall coefficient remains negative when Mg is added to the amorphous $Ni_{40}La_{60}$ and $Cu_{40}Y_{60}$ alloys.[5] Therefore, it has been realized that Al and Mg affect the electronic structure and electron transport in different mechanisms.

Among LT-ET amorphous alloys, the amorphous Cu-Y alloy can dissolve both Al and Mg to a large extent and, hence, may well be suited to extract the role of Al and Mg in a common amorphous matrix. The electron-transport properties have been already studied for a series of the amorphous $Al_x(Cu_{0.4}Y_{0.6})_{100-x}$ and $Mg_x(Cu_{0.4}Y_{0.6})_{100-x}$ ($0 \leqslant x \leqslant 85$) alloys.[6] In the present work, we have employed the same series of amorphous Al-Cu-Y and Mg-Cu-Y alloys and determined both atomic and electronic structures self-consistently by utilizing the neutron-diffraction technique as an atomic structure probe and x-ray photoemission spectroscopy (XPS) and soft x-ray emission spectroscopy (SXS) as the electronic structure probe and discussed the reason why the Al and Mg affect various physical properties in an entirely different manner.

II. EXPERIMENTAL PROCEDURE

$Al_x(Cu_{0.4}Y_{0.6})_{100-x}$ ($0 \leqslant x \leqslant 85$), $Mg_x(Cu_{0.4}Y_{0.6})_{100-x}$ ($0 \leqslant x \leqslant 80$) and $Al_{50}Y_{50}$ alloy ingots were prepared by arc-melting appropriate amounts of pure elements 99.999% Al, 99.9% Mg, 99.99% Cu, and 99.9% Y. The first two series of alloys are hereafter abbreviated as $[Al]_x$ and $[Mg]_x$, respectively. Pure Y metal containing the least oxygen content ($\leqslant$0.4 at. % O) was purchased from Shinetsu Chemicals, LTD, Japan. Furthermore, the hexagonal AlCuY, CsCl-type MgY and C-15-type $MgCu_2$ intermetallic compounds plus fcc $Al_{97}Cu_3$ and $Al_{18}Cu_{82}$ alloys were fabricated for comparison.

Amorphous ribbons were formed in the following alloys, using a single-roll spinning wheel apparatus operated in Ar-gas atmosphere; $[Al]_x$ ($x=0$, 5, 10, 15, 20, 30, 80, and 85), $[Mg]_x$ ($x=10$, 20, 30, 40, 60, and 80) and $Al_{50}Y_{50}$. The x-ray-diffraction measurements with Cu $K\alpha$ radiation revealed that an amorphous single phase region splits into $0 \leqslant x \leqslant 0.3$ and $0.8 \leqslant x \leqslant 0.85$ in the [Al] alloy system, whereas it extends continuously over the range $0 \leqslant x \leqslant 0.8$ in the [Mg] alloy system. The crystallization temperature is measured, using the differential scanning calorimeter (DSC) with a heating rate of 15 K/min. The $Al_{97}Cu_3$ alloy was melt-quenched to ensure the formation of a disordered fcc single phase without any precipitated phase.

The electronic specific-heat coefficient, electrical resistivity and Hall coefficient for the present amorphous $[Al]_x$ and $[Mg]_x$ alloys were already reported elsewhere.[5,6] Only the resistivity and Hall coefficient for the hexagonal AlCuY intermetallic compound were newly measured at 300 K. The data are listed in Table I.

TABLE I. Electron-transport properties of hexagonal AlCuY intermetallic compound.

	$\rho_{300\ K}$ ($\mu\Omega$ cm)	$R_{H300\ K}$($\times 10^{-11}$ m^3/A s)
AlCuY	76	18.9

The XPS valence-band spectra were measured for a series of $[Al]_x$ and $[Mg]_x$ alloys plus the fcc $Al_{97}Cu_3$, using monochromated x rays of the Al $K\alpha$ radiation (Surface Science Instrument X probe). The core levels associated with Al $2p$, Mg $2p$, Cu $3d$, Cu $2p$, and Y $3d$ states are also measured for both $[Al]_x$ and $[Mg]_x$ alloys. The electron-probe microanalyzer (Shimazu, EPMA-8705) equipped with a bent crystal was used to measure the SXS spectra at an accelerating voltage of 10 kV. The Al $K\beta$ and Cu $L\alpha_{1,2}$ spectra were measured for the amorphous $[Al]_x$ alloys, together with the amorphous $Al_{50}Y_{50}$ alloy, the fcc $Al_{18}Cu_{82}$ alloy and pure Al. Similarly, the Mg $K\beta$ and Cu $L\alpha_{1,2}$ spectra were measured for the amorphous [Mg] alloys, MgY and $MgCu_2$ intermetallic compounds and pure Mg.

The Fermi level in the Al $K\beta$ and Mg $K\beta$ spectra were determined by measuring the XPS Al $2p$ and Mg $2p$ core levels and the Al $K\alpha$ and Mg $K\alpha$ spectra, respectively. The Fermi level in the Cu $L\alpha_{1,2}$ spectrum corresponding to the transition from the Cu $3d$ states to the $2p$ level can be determined by measuring the XPS Cu $2p$ core level.

III. RESULTS

A. Thermal properties

Figure 1 shows the DSC thermograms for a series of amorphous $[Al]_x$ and $[Mg]_x$ ($0 \leqslant x \leqslant 85$) alloys. The crystallization temperature T_x, as manifested by an exothermic peak, is plotted in Fig. 2 as a function of Al or Mg concentration. It is clear that the value of T_x increases rapidly up to 30 at. % Al but drops substantially when Al content exceeds 80 at. %. In contrast, the value of T_x in the amorphous [Mg] alloys monotonically decreases over a whole Mg concentration range. This already indicates that Al and Mg atoms play a different role, when dissolved into the amorphous Cu-Y matrix. It is also suggestive that the Al atom, when its concentration is in the range ($0 < x \leqslant 30$), tends to form strong bonding with Cu and Y atoms and strengthens the bonding over the amorphous Cu-Y alloy, but that the Mg atom apparently weakens it on average.

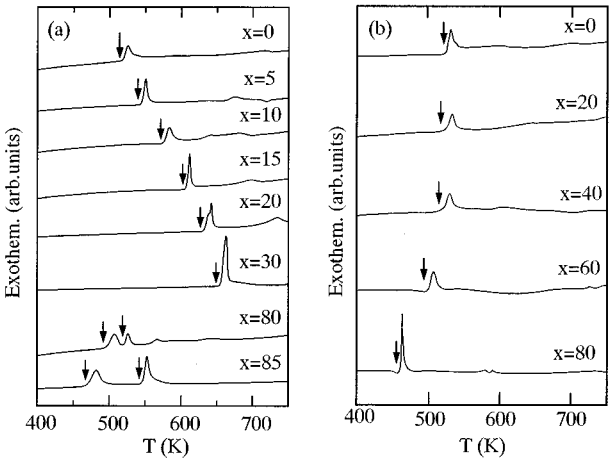

FIG. 1. DSC spectra for a series of amorphous (a) $Al_x(Cu_{0.4}Y_{0.6})_{100-x}$ and (b) $Mg_x(Cu_{0.4}Y_{0.6})_{100-x}$ ($0 \leqslant x \leqslant 85$) alloys.

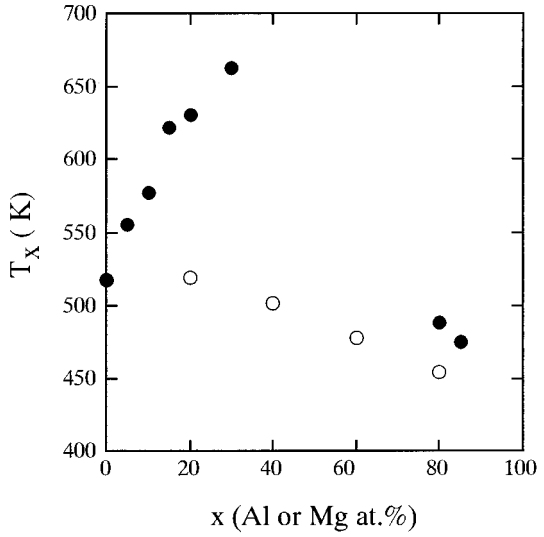

FIG. 2. Crystallization temperature T_x as a function of Al or Mg concentration for amorphous $Al_x(Cu_{0.4}Y_{0.6})_{100-x}$ (●) and $Mg_x(Cu_{0.4}Y_{0.6})_{100-x}$ ($0 \leqslant x \leqslant 85$) (○) alloys.

The crystalline phases formed after being heated up to 770 K were investigated by using x-ray diffraction with Cu $K\alpha$ radiation. The binary $Cu_{40}Y_{60}$ and ternary alloys with $x=10$ and 20 are partitioned into CuY and remaining phases. However, the $[Al]_{30}$ sample is identified as an almost single phase of the hexagonal AlCuY intermetallic compound isostructural to Fe_2P.[8] Similarly, the major diffraction lines of the $[Al]_{80}$ and $[Al]_{85}$ samples can be indexed in terms of the τ_2 phase,[9] which is isostructural to $BaAl_4$.

In the case of the crystallized [Mg] alloys, the CuY compound remains observed up to $x=20$ as a major phase. Pure Mg is definitely precipitated in the crystallized $[Mg]_{80}$ sample. The diffraction lines for the alloys with intermediate Mg concentrations $x=30$ and 40 cannot be indexed in terms of any single phase, as opposed to the $[Al]_{30}$ alloy. Indeed, the scanning electron microscopy micrograph revealed that the crystallized $[Mg]_{30}$ is partitioned into a mixture of Mg-rich and Mg-poor phases. The lattice constant of the resulting CuY compound in both [Al] and [Mg] alloys is plotted in Fig. 3 as a function of Al or Mg concentration. It is seen that the lattice constant increases in the case of [Al] but remains unchanged in [Mg]. This implies that Al atoms are well substituted in the CuY lattice but that Mg atoms are apparently depleted from the CuY compound. All this evidence suggests that the atomic environment and the bonding nature among constituent atoms are substantially different, depending on whether Al or Mg is introduced in the Cu-Y amorphous matrix.

B. Determination of atomic structures

1. Amorphous Cu-Y alloy

Maret *et al.*[10] deduced the atomic structure of the amorphous $Cu_{33}Y_{67}$ alloy by combining both the x-ray and

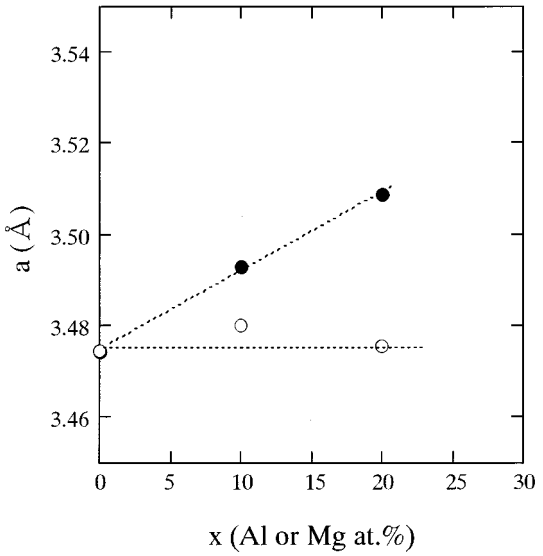

FIG. 3. Lattice constant of the CuY compound phase obtained after crystallization of amorphous $Al_x(Cu_{0.4}Y_{0.6})_{100-x}$ (●) and $Mg_x(Cu_{0.4}Y_{0.6})_{100-x}$ ($0 \leqslant x \leqslant 85$) (○) alloys.

neutron-diffraction techniques. The two different samples, one containing natural Cu and the other ^{63}Cu isotope, were prepared for the neutron-diffraction experiment to determine three partial structure factors $S_{Cu\text{-}Cu}$, $S_{Cu\text{-}Y}$, and $S_{Y\text{-}Y}$. The partial radial distribution function (hereafter abbreviated as RDF) can be deduced by Fourier transforming the partial structure factors. The total RDF, which is reproduced from the literature[10] and included in Fig. 4(a), turned out to consist of two peaks positioned at 2.9 and 3.6 Å. A comparison with the partial RDF led them to conclude that the former originates from the Cu-Y pair and the latter from the Y-Y pair. The Cu-Y distance of 2.9 Å is shorter than the value of 3.08 Å deduced from the hard-sphere model given as a sum of the respective Goldschmidt radii. This indicates that strong bonding states are formed between the Cu and Y atoms. As an additional unique feature, they found that the Cu atom has no direct contact with neighboring Cu atoms.

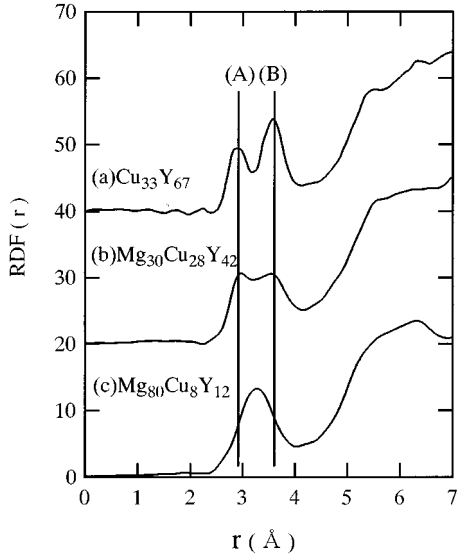

FIG. 4. Total radial distribution function RDF(r) for amorphous $Mg_x(Cu_{0.4}Y_{0.6})_{100-x}$ ($x=30$ and 80) alloys. The data for the amorphous $Cu_{33}Y_{67}$ alloy were reproduced from Maret *et al.* (Ref. 10). Peaks (A) and (B) correspond to the Cu-Y and Y-Y correlations, respectively.

2. Amorphous $[Mg]_x$ alloys

The total RDF spectra for the amorphous $[Mg]_{30}$ and $[Mg]_{80}$ alloys are shown in Fig. 4(b) and 4(c). It is seen that the main peaks (A) and (B) corresponding to the Cu-Y and Y-Y atomic pairs in the binary Cu-Y alloy remain visible in the amorphous $[Mg]_{30}$ alloy. This is consistent with the data shown in Fig. 3, where the lattice constant of the CuY compound phase formed upon crystallization of an amorphous phase, exhibits no Mg concentration dependence. Therefore, we believe that the interaction of Mg atoms with surrounding Cu and Y atoms must be weak.

The RDF spectrum for the amorphous $[Mg]_{80}$ alloy consists of a single peak centered at 3.3 Å. This peak reflects definitely the Mg-Mg pair, as expected from the hard-sphere model. Note here that the Goldschmidt radius for the Mg atom is between those of Cu and Y atoms: $r_{Mg}=1.6$ Å, $r_{Cu}=1.28$ Å, and $r_Y=1.80$ Å. But the broadness of the peak strongly suggests that the Cu-Y and Y-Y correlations still remain at the same position as in the amorphous Cu-Y binary alloy. Therefore, the atomic structure of the amorphous $[Mg]_{80}$ alloy may be viewed as the randomly distributed Mg atoms, in which the Cu-Y clusters may be embedded.

3. Amorphous $[Al]_x$ alloys

The RDF spectra for the amorphous $[Al]_x$ alloys with $x=30$ and 80 are shown in Fig. 5. First of all, it should be noted that the RDF spectra for both $[Al]_{30}$ and $[Al]_{80}$ alloys are asymmetric, as opposed to more symmetric spectra for the [Mg] alloys. This suggests that the local atomic environment in the amorphous [Al] alloys possesses some unique local structure. We noted in Sec. III A that the amorphous $[Al]_{30}$ alloy is crystallized into the hexagonal AlCuY intermetallic compound. According to its crystallographic data,[8] Al-Cu, Cu-Y, Al-Al, Al-Y, Y-Y, and Cu-Cu pairs are found in the distance of 2.54, 2.92, 3.04, 3.25, 3.65, and 4.06 Å, respectively. The distances of the Al-Cu and Cu-Y pairs are shorter than those given by the hard-sphere model, whereas those of Al-Al and Cu-Cu pairs are longer. Particularly, the distribution of Al atoms is somewhat unique. They are always united in three, each Al atom being separated from the other two by 3.04 Å, and exist as a cluster. The Al clusters thus formed are separated from each other by more than 4 Å. Hence, even the intracluster Al-Al distance is much longer than that of 2.86 Å expected from the Al-Al hard-sphere model or the nearest-neighbor distance in fcc Al or liquid Al.

The RDF spectrum for the amorphous $[Al]_{30}$ alloy is now compared with the local atomic structure of the AlCuY intermetallic compound. The position and height of the vertical line represent the distance and relative coordination number of the atomic pairs in the AlCuY compound, respectively. A comparison with the AlCuY compound allows us to identify the local atomic structure in the amorphous $[Al]_{30}$ phase: a small peak at 2.5 Å most likely corresponds to the Al-Cu pair, a shoulder around 2.9 Å to the Cu-Y and Al-Cu pairs, a

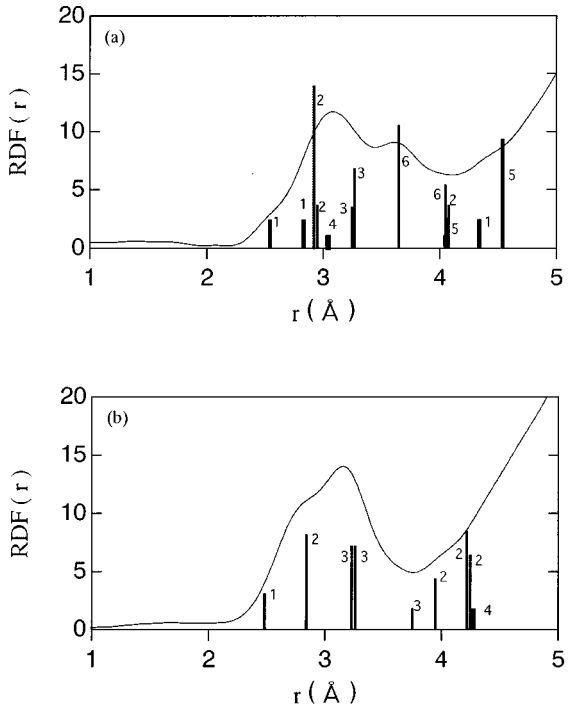

FIG. 5. Total radial distribution function RDF(r) for amorphous (a) $Al_{30}(Cu_{0.4}Y_{0.6})_{70}$ and (b) $Al_{80}(Cu_{0.4}Y_{0.6})_{20}$ alloys. Vertical lines refer to atomic positions of (a) hexagonal AlCuY compound and (b) τ_2 phase compound. Its height is drawn in proportion to the coordination number. The number attached to each vertical line refers to the following: (1) Al-Cu, (2) Cu-Y, (3) Al-Y, (4) Al-Al, (5) Cu-Cu, and (6) Y-Y in the AlCuY compound and (1) Al-Cu, (2) Al-Al, (3) Al-Y, and (4) Y-Y in the τ_2 compound.

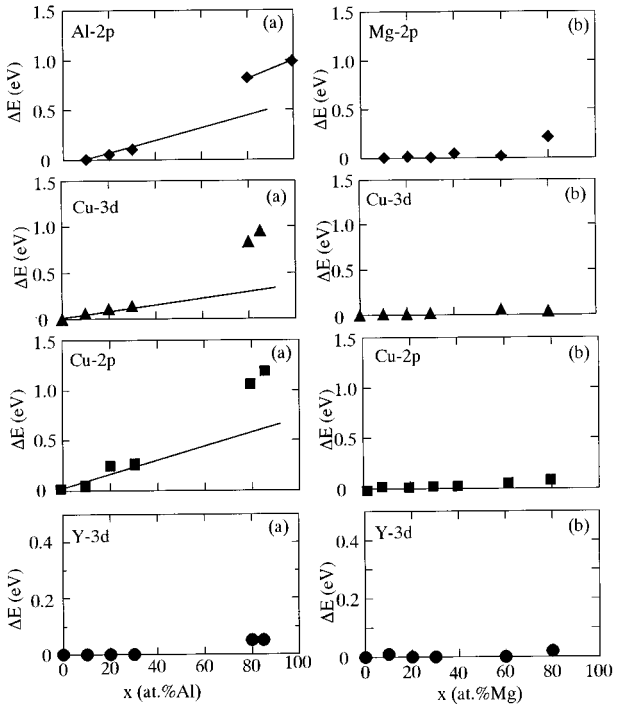

FIG. 6. A shift of the Al 2p, Mg 2p, Cu 3d, Cu 2p, and Y 3d states as a function of Al or Mg concentration in a series of amorphous (a) $Al_x(Cu_{0.4}Y_{0.6})_{100-x}$ and (b) $Mg_x(Cu_{0.4}Y_{0.6})_{100-x}$ ($0 \leqslant x \leqslant 85$) alloys. The data were measured relative to that for the amorphous $Cu_{40}Y_{60}$ alloy. The data for the Al 2p and Mg 2p states were measured relative to that for the $[Al]_{10}$ and $[Mg]_{10}$ alloys, respectively. A positive sign in the shift ΔE indicates an increase in the binding energy relative to the reference.

central peak around 3.2 Å to the Al-Al and Al-Y pairs and a peak around 3.7 Å to the Y-Y pair. We believe from this comparison that the atomic structure of the amorphous $[Al]_{30}$ alloy reflects well the local structure of the AlCuY compound and is characterized by the formation of the Al-Y and Al-Cu nearest-neighbor atomic pairs while there is a lack of the Al-Al and Cu-Cu nearest-neighbor pairs.

Similarly, a comparison is made with the τ_2 phase compound for the amorphous $[Al]_{80}$ alloy. Here a small amount of Cu atoms is assumed to be randomly substituted for Al atoms in the $BaAl_4$ structure. Note that the largest Y atom in the τ_2 phase is completely surrounded by totally 16 Al and Cu atoms[9] and, hence, no Y-Y nearest-neighbor atomic pair exists. By comparing with the atomic structure of the τ_2 phase, we can attribute a finite RDF near 2.5 Å to the Al-Cu pair. The second largest peak observed at 2.8 Å must be attributed to the Al-Al pair, while the largest peak at 3.2 Å to the Al-Y pair. We believe, therefore, that the atomic structure in the amorphous $[Al]_{80}$ alloy reflects well that of the τ_2-phase compound: each Al atom always possesses an Al atom as a nearest neighbor in the close-packed distance, while the Y-Y nearest-neighbor pair no longer exists. The Cu-Cu nearest-neighbor pair would also be scarcely formed because of its low concentration of only 8 at. %. This unique atomic structure must be responsible for the emergence of the free-electron-like electronic structure and free-electron-like transport properties, as will be discussed later.

The x-ray anomalous scattering experiments have been reported by Matsubara *et al.*[11] for the amorphous $Al_{87}Ni_5Y_8$ alloy. They pointed out that large Y atoms are always surrounded by Al atoms and the Al-Al and Al-Y atomic pairs appear at the distances of 2.86 and 3.20 Å, respectively, in good agreement with our conclusion.

C. Determination of electronic structures

1. XPS core levels in amorphous [Al] and [Mg] alloys

The Al 2p, Mg 2p, Cu 2p, and Y 3d core levels were measured for both amorphous $[Al]_x$ and $[Mg]_x$ alloys. Figure 6 shows the Al and Mg concentration dependences of the shift of the core levels relative to those of the amorphous $Cu_{40}Y_{60}$ alloy. The binding energy at the center of the Cu 3d valence band is also included. As far as the Al 2p and Mg 2p core levels are concerned, the data for the $[Al]_{10}$ and $[Mg]_{10}$ are taken as a reference. It can be seen that both Cu 2p and Cu 3d states in the amorphous $[Al]_x$ alloys shift toward higher binding energies with increasing Al concentration but that an extrapolated line drawn through the data points in the range $0 \leqslant x \leqslant 30$ is positioned far below the data in the range $80 \leqslant x \leqslant 85$, indicating a substantial change in the electronic structure across the middle field. The Al 2p level also shows a substantial increase in the shift with increasing Al concentration. Similarly, a shift in the Y 3d level is negligibly small below 30 at. % Al but becomes finite above 80

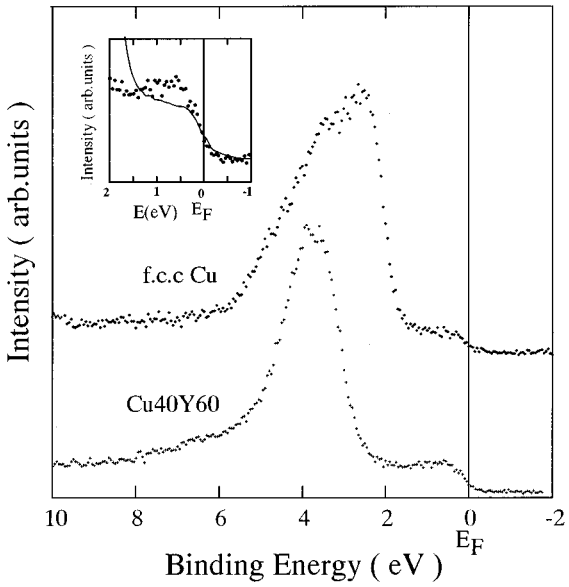

FIG. 7. XPS valence-band spectra for pure Cu and amorphous $Cu_{40}Y_{60}$ alloy. The spectra near the Fermi level are shown on an expanded scale in its inset, where dots and smoothed curve represent the data for $Cu_{40}Y_{60}$ and pure Cu, respectively.

at. % Al. In contrast, a shift in core levels in the amorphous [Mg] alloys is always negligibly small over its whole concentration range.

2. XPS valence-band spectra in amorphous $Cu_{40}Y_{60}$ alloy

The XPS valence-band spectrum for the amorphous $Cu_{40}Y_{60}$ alloy is shown in Fig. 7 in comparison with that of pure Cu. As is well known, a main peak extending over 2–6 eV in pure Cu represents the Cu 3*d* states. According to the band calculations by Hausleitner, Tegze, and Hafner,[12] the valence band of the amorphous $Cu_{35}Y_{65}$ alloy consists of the Cu 3*d* peak at the binding energy of 4 eV and the Y 4*d* band across the Fermi level. Hence, a main peak observed at 3.5 eV in the amorphous $Cu_{40}Y_{60}$ alloy can be easily identified as the Cu 3*d* states. Its center is apparently displaced toward a higher binding energy by about 1 eV relative to pure Cu. In addition, as shown in its inset, we find a small hump immediately below E_F in the amorphous phase, being taken as an evidence for the presence of the Y 4*d* states.

3. XPS valence-band spectra in amorphous [Al] and [Mg] alloys

The XPS valence-band spectra for a series of the amorphous $[Al]_x$ and $[Mg]_x$ alloys are shown in Fig. 8. First of all, it should be noted that the XPS valence-band structure continues to reflect mainly the Cu 3*d* and Y 4*d* states, even when the concentration of the third element Al or Mg is increased in the amorphous Cu-Y matrix. As one of the most striking features, one finds that the Cu 3*d* peak is gradually displaced to higher binding energies in the amorphous [Al] alloys, whereas it remains essentially unchanged in the [Mg] alloys. Included in Fig. 8 are the data for the rapidly quenched fcc $Al_{97}Cu_3$ alloy, in which each Cu atom is believed to be randomly distributed and almost completely surrounded by Al atoms. It is clearly seen from Fig. 8 that the

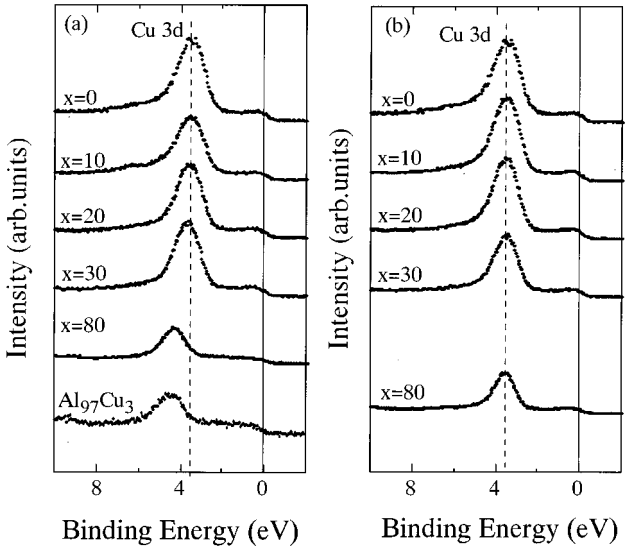

FIG. 8. XPS valence-band spectra for a series of amorphous (a) $Al_x(Cu_{0.4}Y_{0.6})_{100-x}$ and (b) $Mg_x(Cu_{0.4}Y_{0.6})_{100-x}$ ($0 \leqslant x \leqslant 85$) alloys. The data for the fcc $Al_{97}Cu_3$ alloy are also included for comparison.

Cu 3*d* peak in this fcc alloy well coincides in position with that in the amorphous $[Al]_{80}$ alloy. This means that the Cu atom in the $[Al]_{80}$ amorphous alloy has an atomic environment similar to that of the fcc $Al_{97}Cu_3$ alloy and, hence, exists as an isolated impurity by being surrounded with Al atoms.

Unfortunately, the presence of the Y 4*d* states at E_F is scarcely seen in Fig. 8. The XPS spectra immediately below E_F are expanded and shown in Fig. 9. Now it is clear that the Y 4*d* states completely disappear when Al concentration reaches 80 at. % in the amorphous [Al] alloys, but remain finite up to $x=80$ in the amorphous [Mg] alloys. Hence, both Cu 3*d* and Y 4*d* states are apparently displaced in an opposite direction with increasing Al concentration, as if they are

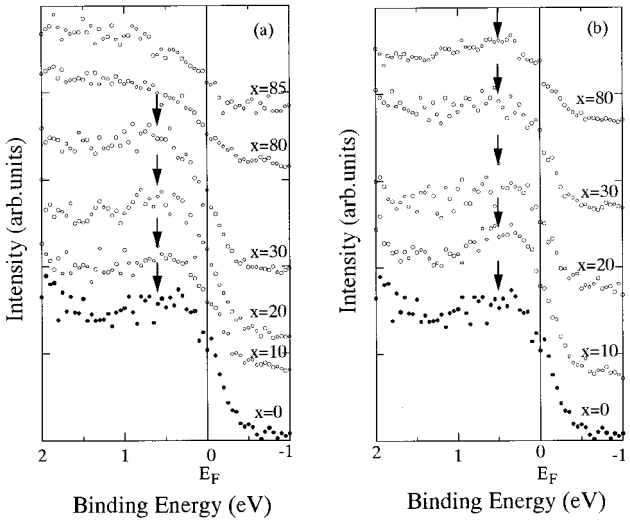

FIG. 9. XPS valence-band spectra (Fig. 8) in the vicinity of the Fermi level are shown on an expanded scale for a series of amorphous (a) $Al_x(Cu_{0.4}Y_{0.6})_{100-x}$ and (b) $Mg_x(Cu_{0.4}Y_{0.6})_{100-x}$ ($0 \leqslant x \leqslant 85$) alloys. Arrow shows a hump, which indicates the presence of the Y 4*d* states.

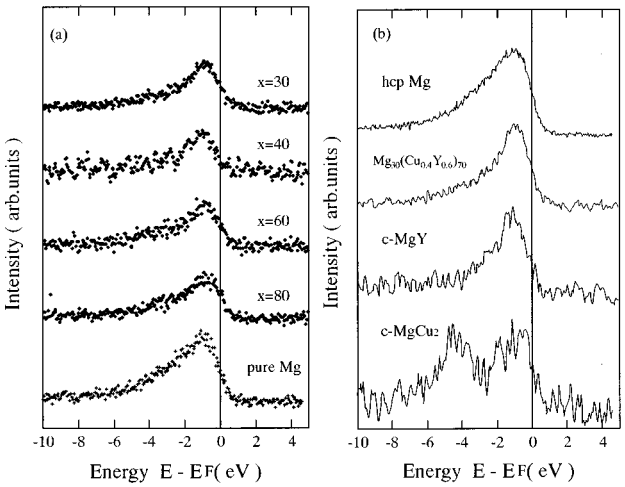

FIG. 10. Mg $K\beta$ SXS spectra for a series of (a) amorphous $Mg_x(Cu_{0.4}Y_{0.6})_{100-x}$ ($0 \leqslant x \leqslant 80$) alloys in comparison with the data for hcp Mg, CsCl-type MgY and C-15-type $MgCu_2$ intermetallic compounds. The binding energy is measured relative to the Fermi level.

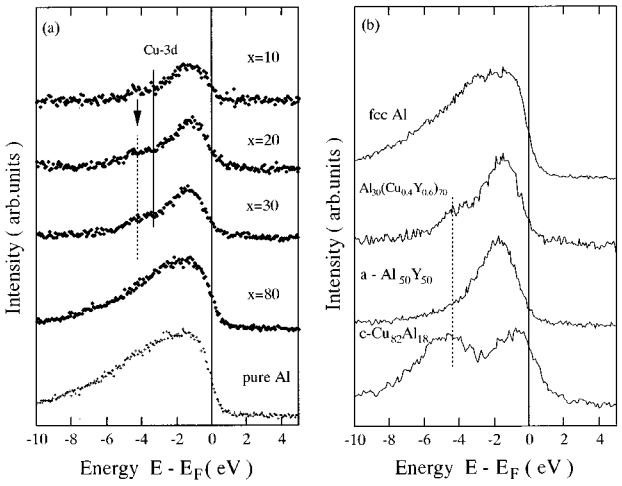

FIG. 11. Al $K\beta$ SXS spectra for a series of (a) amorphous $Al_x(Cu_{0.4}Y_{0.6})_{100-x}$ ($0 \leqslant x \leqslant 80$) alloys in comparison with the data for (b) fcc Al, amorphous $Al_{50}Y_{50}$ and fcc $Al_{18}Cu_{82}$ alloy. The binding energy is measured relative to the Fermi level. Solid vertical line in (a) refers to the center of the Cu $3d$ band deduced from the XPS spectra shown in Fig. 7. A dashed line in (a) and (b) refers to the position of the bonding states formed by the hybridization between Al $3p$ and Cu $3d$ states.

repelled with each other. But no such displacement takes place in the amorphous [Mg] alloys.

This unique alloying effect observed in the XPS valence-band spectra must be reconciled with the atomic structure discussed in the preceding section. We stressed that the Al-Cu and Al-Y nearest neighbor atomic pairs are preferentially formed in the amorphous [Al] alloys. Unique alloying effects as observed in both RDF and XPS valence-band spectra suggest that hybridization in the Al-Cu and the Al-Y atomic pairs may be stronger than that in the Cu-Y atomic pair and would eventually result in the isolation of Cu and Y atoms at high Al concentrations. Instead, a change in the RDF spectra for the amorphous [Mg] alloys can be understood as the gradual growth of the Mg-Mg nearest-neighbor pairs while preserving the Cu-Y atomic pair. The hybridization effect in the Mg-Y and Mg-Cu atomic pairs is probably weaker than in the Cu-Y atomic pair and this leaves the Cu-Y atomic pair even up to high Mg concentrations. In the following sections, we will extract more straightforward information about hybridization effects among various atomic pairs from the measured SXS spectra and specify the electronic states of Al and Mg atoms involved in the hybridization with Cu $3d$ and Y $4d$ states.

4. Mg $K\beta$ SXS spectra in amorphous [Mg] alloys

The Mg $K\beta$ spectrum provides information about the Mg $3p$ electron distribution. The results are shown in Fig. 10 for a series of amorphous $[Mg]_x$ alloys, together with those of pure hcp Mg, MgY, and $MgCu_2$ compounds. It is clear that the spectra for all amorphous [Mg] alloys differ from those of the $MgCu_2$ compound possessing a double peak but more resemble that of the MgY compound. This implies that the Mg $3p$ electrons hybridize with the Y $4d$ electrons but essentially do not with the Cu $3d$ states.

5. Al $K\beta$ SXS spectra in the amorphous [Al] alloys

The Al $K\beta$ SXS spectra, which reflects the Al $3p$ partial density of states, are shown in Fig. 11 for a series of amorphous $[Al]_x$ alloys, together with those for the amorphous $Al_{50}Y_{50}$ alloy, fcc $Al_{18}Cu_{82}$ alloy and fcc Al. First of all, we find that the spectrum for the amorphous $[Al]_{80}$ alloy resembles well that of pure Al, lending support to the possession of the free-electron-like valence-band structure. On the other hand, the spectra in the composition range $10 \leqslant x \leqslant 30$ are much narrower in width than that of pure Al and resemble more that of the amorphous $Al_{50}Y_{50}$ alloy. A reduction in the width of the Al $3p$ electron distribution is taken as an evidence for the presence of strong hybridization between Al $3p$ and Y $4d$ states.

As opposed to the amorphous $Al_{50}Y_{50}$ alloy, however, there exists an additional small hump in the binding energies centered at about 4 eV in the $[Al]_x$ amorphous alloys with $x=20$ and 30. This hump is located at a higher binding energy side of the Cu $3d$ XPS peak, which is marked as a vertical line in Fig. 11. Furthermore, its position agrees well with that of the $Al_{18}Cu_{82}$ alloy. Therefore, we are led to conclude that this small hump represents the bonding states of Al $3p$ electrons as a result of the hybridization with the Cu $3d$ states.

As is clear from the argument above, the Al $K\beta$ spectra clearly demonstrated the presence of strong hybridization between the Al $3p$ and Cu $3d$ states and also between Al $3p$ and Y $4d$ states. It must be also emphasized in Fig. 11 that the population of Al $3p$ electrons at E_F is greatly reduced in the Al-poor amorphous alloys relative to that in pure Al whereas the Al-rich amorphous alloy holds the free-electron-like extended states. This is certainly responsible for an enhancement in the resistivity in the amorphous $[Al]_{30}$ alloy and its subsequent sharp decrease in the Al-rich regime. More details will be discussed in Sec. IV C.

6. Cu $L\alpha_{1,2}$ SXS spectra in amorphous [Al] and [Mg] alloys

The Cu $L\alpha_{1,2}$ SXS spectra are known to reflect mainly the Cu $3d$ states. Figure 12 shows Cu $L\alpha_{1,2}$ spectra for both

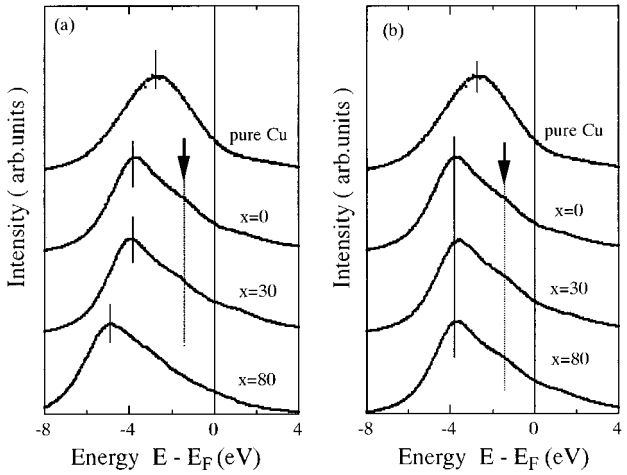

FIG. 12. Cu$L\alpha_{1,2}$ SXS spectra for a series of amorphous (a) $Al_x(Cu_{0.4}Y_{0.6})_{100-x}$ and (b) $Mg_x(Cu_{0.4}Y_{0.6})_{100-x}$ ($0 \leqslant x \leqslant 80$) alloys along with the data for pure Cu. The center of the Cu $3d$ band is marked by a solid line in (a) and (b). A weak hump marked as arrow with dashed line indicates the presence of the Y $4d$ states. It is absent in the amorphous $[Al]_{80}$ alloy.

amorphous [Al] and [Mg] alloys along with that of pure Cu. As compared with the pure Cu, a main peak corresponding to the center of the Cu $3d$ states is shifted by about 1 eV toward higher binding energies in the amorphous $Cu_{40}Y_{60}$ alloy. This is consistent with the shift of the XPS Cu $3d$ states shown in Fig. 7. A shift of the Cu $3d$ states toward further higher binding energies occurs significantly, when Al concentration reaches 80 at. %, whereas it is negligible in the amorphous $[Mg]_{80}$ alloy. This is again consistent with the XPS data shown in Fig. 8. One may further notice the presence of a very weak hump as an additional unique feature in the Cu $L\alpha_{1,2}$ spectra, which is marked by an arrow in both amorphous [Al] and [Mg] alloys. Undoubtedly, this hump is caused by the hybridization with the Y $4d$ states. This hump, though very weak, is visible for all amorphous [Mg] alloys but apparently disappears for the amorphous $[Al]_{80}$ alloy. This is in an excellent agreement with the XPS spectra shown in Fig. 9.

D. Atomic and electronic structures in amorphous [Al] and [Mg] alloys

As discussed above, the SXS spectra certainly provided crucial information about the hybridization effects among various atomic pairs involved. By combining RDF, XPS, and SXS data together, we reach the following conclusions: hybridization of Al $3p$ states with both Cu $3d$ and Y $4d$ states is so strong that the original hybridization between Cu $3d$ and Y $4d$ states is weakened in amorphous [Al] alloys. This is reflected in the RDF spectrum for the $[Al]_{30}$ alloy as the formation of Al-Cu and Al-Y atomic pairs with the absence of the Al-Al nearest-neighbor atomic pair and as a growth of the bonding states of the Al $3p$ states with Cu $3d$ and Y $4d$ states in the Al $K\beta$ spectrum. Strong hybridization eventually results in the isolated Cu and Y atoms in the Al matrix, as the Al concentration exceeds 80 at. %. This is consistent with the observed RDF spectrum and also free-electron-like XPS and SXS spectra. Furthermore, we could point out that

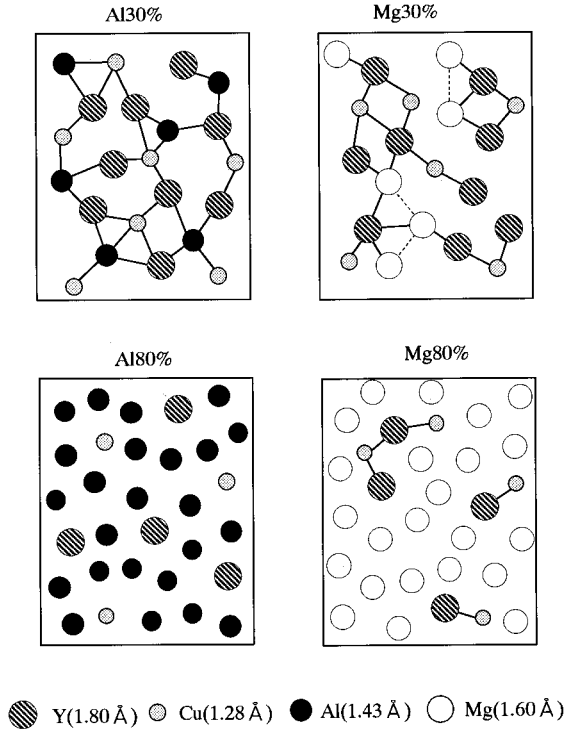

FIG. 13. Schematic illustration of local atomic structures for amorphous $[Al]_x$ ($x=30$ and 80) and $[Mg]_x$ ($x=30$ and 80) alloys.

these unique local atomic structures resemble well those in the nearby intermetallic compounds AlCuY and the τ_2 phase existing in the equilibrium phase diagram.[8,9]

In contrast, hybridization of the Mg $3p$ states, particularly with Cu $3d$ states, is so weak that hybridization between Cu $3d$ and Y $4d$ remains up to the highest Mg concentration. Indeed, a series of the observed RDF spectra for the amorphous [Mg] alloys can be simply interpreted as the sum of the Cu-Y, Y-Y, and Mg-Mg pairs. The XPS and SXS spectra were also successfully interpreted along this line.

Our conclusion for the local atomic structure and valence-band structure in amorphous $[Al]_x$ and $[Mg]_x$ alloys with $x=30$ and 80 may be schematically illustrated in Figs. 13 and 14, respectively. In the next section, we will discuss various physical properties on the basis of atomic and electronic structures thus determined.

IV. A. DISCUSSION

A. Crystallization temperature

The crystallization temperature T_x shown in Fig. 2 certainly reflects the bonding strength of atom pairs in an amorphous phase. As was emphasized, Al atoms in the amorphous $[Al]_{30}$ alloy form a preferential bonding with Cu and Y atoms and the local atomic structure resembles that of the AlCuY intermetallic compound. A resemblance of the local atomic structure to the AlCuY compound, though its melting point has not been reported, is most likely responsible for a sharp increase in T_x in the amorphous $[Al]_{30}$ alloy. However, when the Al concentration is increased, the number of direct Al-Al bonding increases and the free-electron-like electronic structure emerges. This obviously leads to a sharp decrease

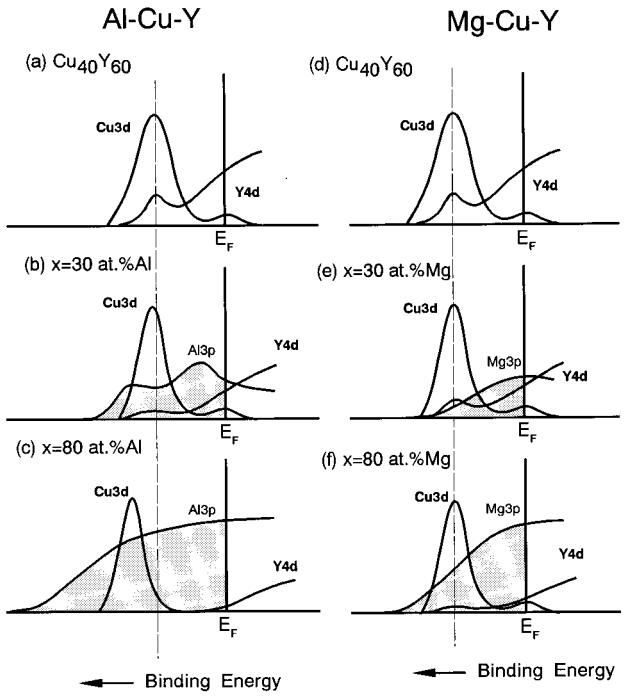

FIG. 14. Schematic illustration of valence-band structures for amorphous $[Al]_x$ ($x=30$ and 80) and $[Mg]_x$ ($x=30$ and 80) alloys.

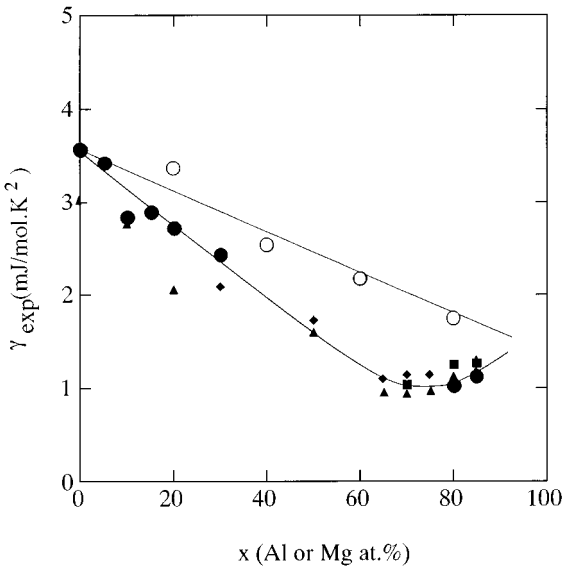

FIG. 15. Al or Mg concentration dependence of the measured electronic specific-heat coefficient $\gamma_{\rm exp}$ for both amorphous $Al_x(Cu_{0.4}Y_{0.6})_{100-x}$ (●) and $Mg_x(Cu_{0.4}Y_{0.6})_{100-x}$ ($0\leqslant x\leqslant 85$) (○) alloys. The literature data for the amorphous $Al_x(Ni_{0.67}M_{0.33})_{100-x}$ alloys with $M=$Ti (◆), Zr (▲), and La (■) are also included (Refs. 4 and 6).

in T_x. Instead, Mg atom simply dilutes the concentration of Cu and Y atoms and contributes to reduce the bonding strength between Cu and Y atoms in proportion to the Mg concentration. This explains why T_x decreases almost linearly with increasing Mg concentration, as shown in Fig. 2.

B. Electronic specific-heat coefficient

The Al or Mg concentration dependence of the measured electronic specific-heat coefficient $\gamma_{\rm exp}$ is plotted in Fig. 15 for both amorphous $[Al]_x$ and $[Mg]_x$ alloys.[5,6] The data for the amorphous $Al_x(Ni_{0.67}M_{0.33})_{100-x}$ alloys with $M=$Ti, Zr, and La are also included.[4] The behavior in the amorphous [Mg] alloys is simple: the value of $\gamma_{\rm exp}$ decreases almost linearly and approaches with increasing Mg concentration that of the more or less free-electron-like hcp Mg ($\gamma_{\rm exp}=1.30$ mJ/mol K^2). As shown in Figs. 8 and 9, both Cu $3d$ and Y $4d$ states in the amorphous [Mg] alloys uniformly reduce their magnitudes without altering their positions. Hence, a change in the band structure with increasing Mg concentration is simply interpreted as the dilution effect without having substantial chemical bonding effect or band-structure effect between Mg and the transition-metal elements Cu and Y. An increase in the Mg concentration results in a decrease in the Y concentration, which in turn reduces the Y $4d$ density of states at E_F. This occurs in proportion to the Y concentration. Hence, a linearly decreasing $\gamma_{\rm exp}$ in the amorphous [Mg] alloys can be explained essentially in terms of the dilution effect described above.

The behavior in the amorphous [Al] alloys is different. The value of $\gamma_{\rm exp}$ decreases much faster and gives rise to a minimum at about $x=70$ with a subsequent gradual increase toward the value of pure Al ($\gamma_{\rm exp}=1.348$ mJ/mol K^2). An initial steep decrease in $\gamma_{\rm exp}$ cannot be explained simply in terms of the dilution effect discussed for the [Mg] alloys but has to be attributed to an additional band-structure effect. As emphasized above, the Y $4d$ states dominate at E_F in the amorphous $Cu_{40}Y_{60}$ alloy but the hybridization between Cu $3d$ and Y $4d$ states is weakened because of the formation of stronger hybridization with the Al $3p$ states. This causes the Y $4d$ states to be displaced to a lower binding energy, while the Cu $3d$ states to a higher binding energy with increasing Al concentration. Therefore, the initial steep decrease in $\gamma_{\rm exp}$ can be attributed to the displacement in the Y $4d$ states to a lower binding energy as a result of weakening of the Cu $3d$ and Y $4d$ hybridization. The free-electron-like electronic structure emerges above $x=70$. Here small $\gamma_{\rm exp}$ values in the neighborhood of 1 mJ/mol K^2, a gradual increase in $\gamma_{\rm exp}$ with increasing Al concentration and an agreement of the extrapolated value with that of pure Al are all consistent with the free-electron-like behavior. We consider this to be realized when the main Y $4d$ states are displaced above E_F and only its small tail remains below E_F, as illustrated in Fig. 14(c). We conclude, therefore, that strong hybridization of the Al $3p$ states with the Y $4d$ and Cu $3d$ states yields the observed steep declining slope in $\gamma_{\rm exp}$ with the subsequent upturn in the amorphous [Al] alloys.

C. Electron-transport properties

Figures 16(a) and 16(b) show the Mg (or Al) concentration dependence of the electrical resistivity at 300 K and the Hall coefficient R_H in amorphous [Al] and [Mg] alloys,[5,6] along with the data for other Mg- and Al-based LT-ET amor-

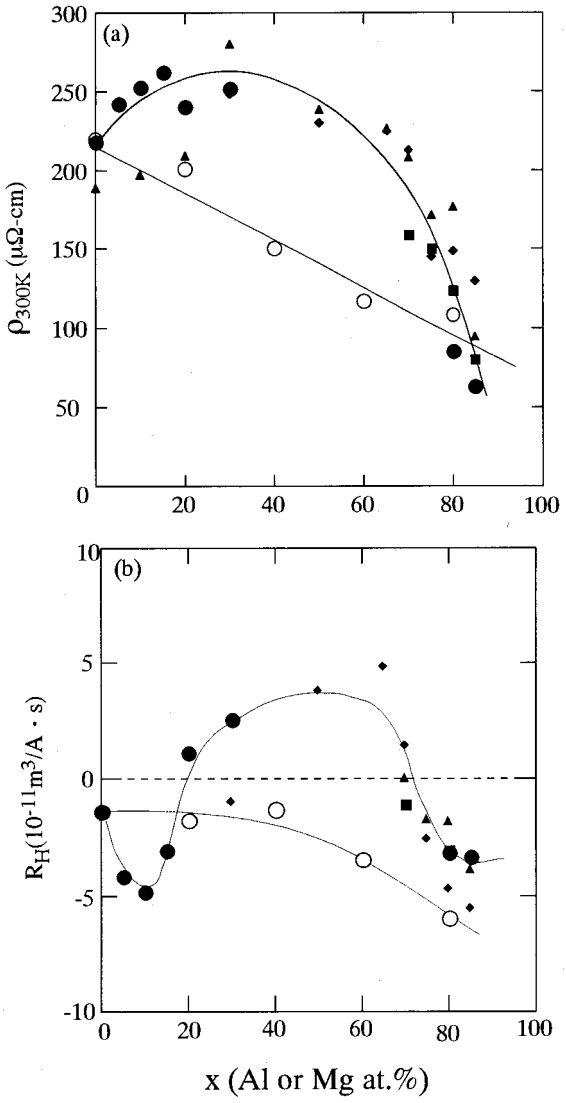

FIG. 16. Al or Mg concentration dependence of the electrical resistivity at 300 K and the Hall coefficient R_H for both amorphous $Al_x(Cu_{0.4}Y_{0.6})_{100-x}$ (●) and $Mg_x(Cu_{0.4}Y_{0.6})_{100-x}$ ($0 \leqslant x \leqslant 85$) (○) alloys. The literature data for the amorphous $Al_x(Ni_{0.67}M_{0.33})_{100-x}$ alloys with M=Ti (◆), Zr (▲), and La (■) are also included (Refs. 4 and 6).

phous alloys.[3,4] It is clear from Fig. 16(a) that, regardless of the combinations of LT and ET, the resistivity increases with increasing Al up to 40 at. % and then drops sharply with further increase in Al concentration. This is in sharp contrast to the behavior in the amorphous Mg-based alloys, where the resistivity consistently decreases with increasing Mg concentration.

We discussed in Sec. IV B that the chemical bonding effect is small and only the dilution effect dominates in the amorphous [Mg] alloys. As illustrated in Fig. 13, the tendency for the formation of Mg atom clusters increases with increasing Mg concentration and serves as opening the sp-electron conduction channel in the amorphous matrix in proportion to the amount of Mg atoms added. This will explain the observed linear decrease in resistivity in the amorphous [Mg] alloys.

The band-structure effect is substantial in the amorphous [Al] alloys. It was shown in Fig. 11 that only a limited amount of the Al $3p$ electrons remains at E_F in the amorphous $[Al]_{30}$ alloy. This implies that Al $3p$ electrons cannot behave in the free-electron fashion in the Al-poor concentration range. Instead, a reduction in Al $3p$ electrons at E_F would result in an enhancement in their effective mass and, in turn, a reduction in the Fermi velocity. Thus, we consider the remaining Al $3p$ electrons at E_F to be indistinguishable from the Y $4d$ electrons as carriers and to be regarded as a part of the Y $4d$ electrons in the following discussion, as far as the Al concentration is lower than $x=40$.

The residual resistivity ρ_0 is related to the density of states at E_F, $N(E_F)$ through the well-known Drude expression:

$$\rho_0^{-1}=\frac{e^2}{3}\Lambda_F v_F N(E_F), \tag{1}$$

where Λ_F and v_F are the mean free path and Fermi velocity of the electrons at E_F. A possible minimum value for the metallic conduction is set to be 0.25 cm^2/s for the diffusion coefficient defined as the product $D=1/3\Lambda_F v_F$.[1] A hyperbolic curve with $D=0.25$ cm^2/s drawn in the ρ-γ diagram is called the high-resistivity limiting curve indicating a possible limit in the metallic conduction. A set of ρ-γ values falls close to the so-called high-resistivity limiting curve, when d-electron conduction dominates. Under such circumstances, the residual resistivity is inversely proportional to the density of states at E_F. Furthermore, the temperature dependence of resistivity in these high-resistivity amorphous alloys can be well characterized by the weak localization effect coupled with the enhanced electron-electron interaction.[1]

As shown in Fig. 17, the present data for the amorphous $[Al]_x$ ($x \leqslant 30$) alloys form the curve parallel and close to the high-resistivity limiting curve. All Al-poor Al-LT-ET amorphous alloys meet this condition and their electron-transport properties are characterized by the weak localization effect.[5,6] As discussed in the preceding section, a steep decrease in the γ_{exp} with increasing Al concentration originated from a decrease in number of Y $4d$ electrons at E_F, which are totally responsible for electron conduction. Therefore, a reduction in the density of states at E_F must be responsible for an increase in resistivity up to $x=40$ in the amorphous [Al] alloys.

We found that the Al atom, when its concentration is low, plays the same role as metalloid elements like B and Si in transition-metal–metalloid-type amorphous alloys. However, in the case of Al, its concentration can be increased up to 85 at. % without losing the glass-forming ability. An increase in Al concentration results in the isolation of the transition-metal elements from each other and gives rise to the growth of the Al-Al nearest-neighbor atomic pairs. An isolation of both Cu and Y atoms in the Al matrix causes the Cu $3d$ states to displace to a higher binding energy and Y $4d$ states above E_F. This promises the emergence of the free-electron-like band structure in the Al-rich regime and explains a drastic drop in the resistivity in Fig. 16(a), when the Al concentration exceeds about $x=70$.

The data for the $[Al]_{80}$ and $[Al]_{85}$ alloys in the ρ-γ plot in Fig. 17 deviate downwards substantially from the limiting curve, signaling a transition from d- to sp-electron conduc-

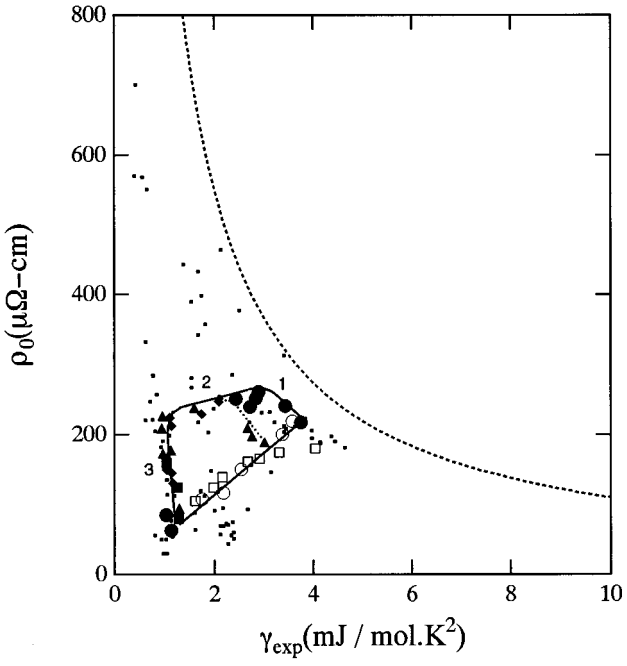

FIG. 17. $\rho-\gamma_{exp}$ diagram for both amorphous $Al_x(Cu_{0.4}Y_{0.6})_{100-x}$ (●) and $Mg_x(Cu_{0.4}Y_{0.6})_{100-x}$ ($0\leqslant x\leqslant 85$) (○) alloys, together with the data for the amorphous $Al_x(Ni_{0.67}M_{0.33})_{100-x}$ alloys with M=Ti (◆), Zr (▲), and La (■) and $Mg_x(Ni_{0.4}La_{0.6})_{100-x}$ alloys (□) (Refs. 4 and 6). Small dots also represent the data for various nonmagnetic amorphous alloys (Refs. 1 and 4). The data for the amorphous $Al_x(Ni_{0.67}M_{0.33})_{100-x}$ alloys with $x=0$ appear at a different point in the diagram, since the concentration of the early transition-metal element M is only 33 at. % and, thus, is lower than 60 at. % Y in the present sample. The data for the amorphous [Mg] alloys fall on a straight line, whereas those for the amorphous [Al] alloys fall into three different regimes: (1) d conduction regime, (2) intermediate regime, and (3) sp conduction regime. A dashed curve represents a high-resistivity limiting curve. See more details in Ref. 1.

tion. In contrast, the data for the amorphous [Mg] alloys constitute an almost straight line with a positive slope. This suggests that the sp-electron conduction channel develops in proportion to the Mg concentration at the expense of the d-electron conduction associated with Y $4d$ states.

The behavior of the Hall coefficient R_H is more dramatic. As shown in Fig. 16(b), a positive R_H appears in the Al-based amorphous alloys, whereas it remains negative in the Mg-based amorphous alloys. A rapid increase in the Hall coefficient towards a positive sign is a characteristic feature observed in the amorphous Al-LT-ET alloys. Several models have been proposed[13,14] but the origin of a positive Hall coefficient in nonmagnetic amorphous alloys has not been well understood. Here we draw attention to the fact that the amorphous $[Al]_{30}$ alloy exhibited a positive Hall coefficient. As discussed in Sec. III B 3 its local atomic structure resembles well the hexagonal AlCuY intermetallic compound with a positive Hall coefficient. Therefore, we believe that the occurrence of a positive Hall coefficient is deeply related to the unique local atomic structure which, in turn, determines the electronic structure near E_F. In the case of the amorphous $[Al]_{30}$ alloy, therefore, the determination of the electronic structure, particularly, the hybridization effect between Al $3p$ and Y $4d$ states in the vicinity of E_F must be important in understanding the origin of a positive Hall coefficient.

D. Interplay of the atomic and electronic structure

To deepen the understanding of the scattering mechanism further, one should calculate both atomic and electronic structures of these ternary amorphous alloys in a manner consistent with all experimental data shown in this work. Firstly, the atomic structures of the amorphous $[Al]_x$ and $[Mg]_x$ ($x=30$ and 80) alloys must be constructed in the molecular-dynamics, simulations to reproduce well the observed RDF spectra. We consider this to be accomplished by using the AlCuY intermetallic compound and τ_2 phase as starting materials for the amorphous $[Al]_x$ ($x=30$ and 80) alloys, respectively. The electronic structure is then calculated in the linear muffin-tin orbital-recursion method. Here the results must be checked if they conform well with the observed electronic structure. We hope that calculations of the electron-transport properties then become feasible on the basis of the electronic structure thus obtained.

ACKNOWLEDGMENTS

We are grateful to Professor Y. Yamada, Nagoya University, and Professor H. Sato, and Professor T. Matsuda, Aichi University of Education, for valuable discussions during the course of this study. We also thank Professor N. Tanaka, Nagoya University, for taking the transmission-electron micrograph and its analysis for the crystallized $[Mg]_{30}$ alloy. One of the authors (U.M.) acknowledges Dr. M. Motoyama, Hyogo Industrial Research Center, for his kind help with the SXS measurement for samples in the early stage of this work.

[1] U. Mizutani, Phys. Status Solidi B **176**, 9 (1993); U. Mizutani, *Material Science Technology A Comprehensive Treatment*, edited by K. W. Cahn, P. Haasen, and E. J. Kramer (VCH, Weinheim, 1993), Vol. 3, Chap. 9, pp. 97–157.

[2] M. Matsuura, Y. Yamada, and U. Mizutani, J. Non-Cryst. Solids **122**, 45 (1990).

[3] Y. Yamada, Y. Itoh, U. Mizutani, N. Shibagaki, and K. Tanaka, J. Phys. F **17**, 2303 (1987).

[4] U. Mizutani, S. Ohashi, T. Matsuda, K. Fukamichi, and K. Tanaka, J. Phys. Condens. Matter **2**, 541 (1990).

[5] U. Mizutani, K. Tanaka, T. Matsuda, N. Suzuki, T. Fukunaga, Y. Ozaki, Y. Yamada, and K. Nakayama, J. Non-Cryst. Solids **156-158**, 297 (1993).

[6] U. Mizutani, H. Sugiura, and Y. Yamada, Mater. Sci. Eng. A **179/180**, 132 (1994).

[7] Y. Yamada, Y. Itoh, T. Matsuda, and U. Mizutani, J. Phys. F **17**, 2313 (1987).

[8] A. E. Dwight, M. H. Muller, R. A. Conner, J. W. Downey, and H.

Knott, Trans. Metall. **242**, 1968 (1968).
[9] O. S. Zarechnyuk and I. F. Kolobnev, Izv. Acad. Nauk SSSR Metall. **5**, 208 (1968).
[10] M. Maret, P. Chieux, P. Hicter, M. Atzmon, and W. L. Johnson, J. Phys. F **17**, 315 (1987).
[11] M. Matsubara, Y. Waseda, A. Inoue, H. Ohtera, and T. Masumoto, Z. Naturforsch. **44a**, 814 (1989).
[12] C. Hausleitner, M. Tegze, and J. Hafner, J. Phys. Condens. Matter **4**, 9557 (1992).
[13] M. Itoh, A. Ishida, S. Tanimori, and H. Sato, Matter. Sci. Eng. A **181/182**, 911 (1994).
[14] D. Nguen-Mahn, D. Mayou, G. J. Morgan, and A. Pasturel, J. Phys. F **17**, 999 (1987).